Ocean Radiant Heating. Part I: Optical Influences

J. CARTER OHLMANN

Scripps Institution of Oceanography, University of California, San Diego, La Jolla, California

DAVID A. SIEGEL

Institute for Computational Earth System Science, Department of Geography, and Donald Bren School of Environmental Science and Management, University of California, Santa Barbara, Santa Barbara, California

CURTIS D. MOBLEY

Sequoia Scientific Inc., Mercer Island, Washington

(Manuscript received 27 July 1998, in final form 8 April 1999)

ABSTRACT

Radiative transfer calculations are used to quantify the effects of physical and biological processes on variations in the transmission of solar radiation through the upper ocean. Results indicate that net irradiance at 10 cm and 5 m can vary by 23 and 34 W m^{-2}, respectively, due to changes in the chlorophyll concentration, cloud amount, and solar zenith angle (when normalized to a climatological surface irradiance of 200 W m^{-2}). Chlorophyll influences solar attenuation in the visible wavebands, and thus has little effect on transmission within the uppermost meter where the quantity of near-infrared energy is substantial. Beneath the top few meters, a chlorophyll increase from 0.03 to 0.3 mg m^{-3} can result in a solar flux decrease of more than 10 W m^{-2}. Clouds alter the spectral composition of the incident irradiance by preferentially attenuating in the near-infrared region, and serve to increase solar transmission in the upper few meters as a greater portion of the irradiance exists in the deep-penetrating, visible wavebands. A 50% reduction in the incident irradiance by clouds causes a near 60% reduction in the radiant heating rate for the top 10 cm of the ocean. Solar zenith angle influences transmission during clear sky periods through changes in sea-surface albedo. This study provides necessary information for improved physically and biologically based solar transmission parameterizations that will enhance upper ocean modeling efforts and sea-surface temperature prediction.

1. Introduction

The thermal and dynamical evolution of the upper ocean is sensitive to the vertical distribution of the solar energy available for ocean radiant heating (Denman 1973; Simpson and Dickey 1981; Charlock 1982; Kantha and Clayson 1994; Schneider et al. 1996; Brainerd and Gregg 1997; Ohlmann et al. 1998). A 10 W m^{-2} change in the quantity of solar radiation absorbed within a 10-m layer can result in a temperature change of more than 0.6°C $month^{-1}$. Simpson and Dickey (1981) reported a 0.5°C change in mixed layer temperature over a 24-h period due to alteration of the solar attenuation coefficient. Such sensitivity to radiant heating processes demonstrates the need for upper ocean models that accurately represent the spatial and temporal variability in solar radiation transmission.

Variations in solar transmission have been described primarily by Jerlov water type (Jerlov 1976), a subjective integer index used to indicate water turbidity, despite the continuous nature of solar attenuation (e.g., Kraus 1972; Paulson and Simpson 1977; Zaneveld and Spinrad 1980; Paulson and Simpson 1981; Woods et al. 1984; Simonot and Le Treut 1986). Models that rely upon continuous, measurable, physical and biological quantities on which solar transmission depends have been developed only recently (e.g., Morel 1988; Morel and Antoine 1994; Ohlmann et al. 1996). These models use the upper ocean chlorophyll concentration and, in one case, the cosine of the zenith angle of the in-water light field to describe solar attenuation. The models have been built upon existing bio-optical parameterizations because data sets with coincidentally measured optical, physical, and biological parameters are limited (cf. Smith and Baker 1978; Morel 1988).

To further improve ocean radiant heating rate parameterizations, a thorough understanding of relationships be-

Corresponding author address: Dr. Carter Ohlmann, Scripps Institution of Oceanography, University of California, San Diego, 9500 Gilman Dr., Code 0230, La Jolla, CA 92093-0230.
E-mail: cohlmann@ucsd.edu

tween solar transmission and the factors that regulate its variations must be developed. Chlorophyll concentration, cloud amount, solar zenith angle, and wind speed all influence solar transmission by altering the in-water solar flux divergence and the sea surface albedo. The quantity of attenuating materials, generally inferred from chlorophyll *a* concentration, has been shown to be the primary regulator of in-water solar transmission on mixed layer depth scales (Smith and Baker 1978; Siegel and Dickey 1987; Morel 1988; Lewis et al. 1990; Siegel et al. 1995; Ohlmann et al. 1998). However, the effect of chlorophyll biomass on solar transmission within the upper few meters (where a significant portion of solar energy exists outside the visible wavebands) is not well characterized. Clouds play a role in shaping the spectral composition of the incident irradiance (Nann and Riordan 1991; Ohlmann et al. 1996; Siegel et al. 1999) and influence the geometry of the incident light field (Liou 1980). A recent study by Siegel et al. (1999) shows the radiant heating rate for the upper 10 cm of the ocean, normalized by the total incident irradiance, can decrease by 50% in the presence of clouds. Solar zenith angle can affect transmission through changes in the light field geometry. Dependence of the vertical decay of irradiance on sun angle has been illustrated for clear sky conditions using Monte Carlo simulations (Kirk 1984; Gordon 1989). Solar zenith angle and wind forcing of the sea surface have been shown to effect in-water radiative transfer through modification of the surface albedo (Payne 1972; Simpson and Paulson 1979; Katsaros et al. 1985; Priesendorfer and Mobley 1986). The relationships between solar transmission and chlorophyll concentration, cloud index, solar zenith angle, and wind speed must be quantified to determine the proper set of parameters for improved solar transmission parameterizations.

The Tropical Ocean Global Atmosphere–Coupled Ocean Atmosphere Response Experiment (TOGA COARE) was conducted to improve the understanding of the coupled ocean–atmosphere system in the western equatorial Pacific warm water pool (WWP; Webster and Lukas 1992). During TOGA COARE, surface incident radiation and in-water spectral irradiance profiles were recorded to directly determine solar transmission at depths beyond ~10 m (Siegel et al. 1995). The TOGA COARE irradiance measurements show the net solar flux at 10 m ranges from 10% to 40% of the surface incident irradiance (Ohlmann et al. 1998). This corresponds to an absolute flux range of 60 W m^{-2}, based on the mean incident irradiance for the TOGA COARE period (~200 W m^{-2}; Weller and Anderson 1996). Solar transmission variations can significantly affect the evolution of SST in regions of high insolation and low wind speeds such as the WWP (Wijesekera and Gregg 1996; Cronin and McPhaden 1997; Ohlmann et al. 1998).

Here, modeled profiles of in-water irradiance are used to address variations in solar transmission associated with changes in upper-ocean chlorophyll concentration, cloud amount, solar zenith angle, and wind speed. This study complements the existing TOGA COARE work by addressing solar transmission within the upper 10 m, and by isolating the roles of the individual factors that regulate transmission. This work is necessary to determine solar transmission variations that can exist on cool-skin and warm-layer depth scales, and to identify the set of independent variables necessary for proper explanation of these variations (e.g., Fairall et al. 1996a,b; Ohlmann et al. 1998). This is a logical next step toward development of improved radiant heating parameterizations for use in upper ocean models. A companion paper (Ohlmann and Siegel 2000) uses the present results to develop a physically and biologically based solar transmission parameterization that accurately resolves the near-surface layer of the ocean and can be used in all conditions and for all locations.

2. The radiative transfer model

a. Model description

The HYDROLIGHT radiative transfer numerical model solves the radiance transfer equation for a plane-parallel environment. A complete description of HYDROLIGHT is given in Mobley (1994); only a brief outline of its basic form and changes made for the present application are given here. The spectral radiance $L(z, \theta, \phi, \lambda)$ provides a complete description of the in-water light field as a function of depth (z), direction (θ, ϕ) and wavelength (λ), and can be used to compute net irradiance profiles, $E_n(z)$, the quantity of interest. HYDROLIGHT computes spectral radiance throughout a water body by solving the one-dimensional, source-free radiance transfer equation

$$\cos\theta \frac{dL(z, \theta, \phi, \lambda)}{dz} = -c(z, \lambda)L(z, \theta, \phi, \lambda) + \int_{\Xi} L(z, \theta', \phi', \lambda)\beta(z, \theta', \phi' \rightarrow \theta, \phi, \lambda) \sin\theta' \, d\theta' \, d\phi', \quad (1)$$

where $c(z, \lambda)$ is the beam attenuation coefficient and $\beta(z, \theta', \phi' \rightarrow \theta, \phi, \lambda)$ is the volume scattering function, which describes scattering from direction θ', ϕ' to direction θ, ϕ. The radiative transfer equation represents the depth change in spectral radiance as a sum of the radiance which is absorbed or scattered out of the path (attenuated), and the radiance scattered into the path from other directions. For the purpose of computing

radiant heating rates, contributions to the radiance by internal sources (such as bioluminescence) and by inelastic scattering can be neglected.

To solve the radiative transfer equation HYDROLIGHT discretizes the set of all directions, Ξ, into a finite set of quadrilateral regions, or quads, bounded by lines of constant θ and ϕ. Here, 24 lines of constant ϕ ($0 \le \phi \le 2\pi$; 15° intervals) and 20 lines of constant θ($0 \le \theta \le \pi$; 10° intervals with two polar caps) are used. Such a partitioning scheme is adequate for resolving changes in solar zenith angle and for the introduction of diffuse light due to clouds. When this directional discretization is applied to the radiance equation [Eq. (1)] the fundamental quantity computed by HYDROLIGHT becomes the radiance averaged over each quad. Integration over all directions in Eq. (1) becomes a sum over all quads. Wavelength is similarly decomposed into finite wavelength bands. Invariant imbedding theory is used to reduce the set of equations for the quad- and band-averaged radiance to a set of Riccati differential equations governing transmittance and reflectance functions. Solution of these differential equations eventually gives the spectral radiance as a function of depth, direction, and wavelength. The net irradiance profile [$E_n(z)$], defined as the difference between downwelling and upwelling irradiance [$E_n(z) = E_d(z) - E_u(z)$], is then computed from spectral radiance using

$$E_d(z) = \int_\lambda \int_{\phi=0}^{2\pi} \int_{\theta=0}^{\pi/2} L(z, \theta, \lambda)|\cos\theta| \sin\theta \, d\theta \, d\phi \, d\lambda \tag{2a}$$

and

$$E_u(z) = \int_\lambda \int_{\phi=0}^{2\pi} \int_{\theta=\pi/2}^{\pi} L(z, \theta, \phi, \lambda)|\cos\theta| \sin\theta \, d\theta \, d\phi \, d\lambda. \tag{2b}$$

Inputs to HYDROLIGHT are absorption and scattering properties of the water column, which determine $c(z, \lambda)$ and $\beta(z, \theta', \phi' \rightarrow \theta, \phi, \lambda)$ in Eq. (1) the radiance distribution incident at the sea surface; and the wind speed, from which the sea surface roughness is computed. The standard version of HYDROLIGHT, which works from 350 to 700 nm, was modified to resolve the solar spectrum from 250 to 2500 nm. This requires the addition of absorption and scattering properties for the added ultraviolet and near-infrared wavebands. Total absorption and scattering are determined by summing the absorption and scattering coefficients for pure water and for chlorophyll biomass.

Pure-water absorption and scattering values are taken from Smith and Baker (1981) for wavelengths between 250 and 800 nm. Beyond 800 nm, pure-water absorption is computed from the complex index of refraction for water given by Hale and Querry (1973). The pure water absorption spectra is shown in Fig. 1a. Pure-water scattering coefficients in the ultraviolet and near-infrared spectral regions are extrapolated from the Smith and Baker values using a $\lambda^{-4.32}$ relationship. The result is shown in Fig. 1b.

Particulate absorption in the visible wavelengths is determined from chlorophyll concentration following the parameterization of Morel (1991), which takes into consideration absorption due to dissolved substances that presumably covary with chlorophyll (Prieur and Sathyndranath 1981; Morel 1991). Particulate and dissolved organic material absorption in the ultraviolet is determined by linearly extrapolating the chlorophyll-specific absorption spectra of Prieur and Sathyndranath (1981) from 400 down to 250 nm. Only pure-water absorption is considered for wavelengths greater than 700 nm where dissolved and particulate absorption are of little consequence (Prieur and Sathyndranath 1981; Morel 1991). The particulate absorption spectra used by HYDROLIGHT are shown in Fig. 1c for three different chlorophyll concentrations.

Particulate scattering for the visible wavelengths is parameterized from chlorophyll concentration using the Gordon and Morel (1983) model. Values are extended to the ultraviolet and near-infrared wavebands with a λ^{-1} relationship. Figure 1d shows the resulting scattering coefficients for three different chlorophyll concentrations.

The volume scattering function used by HYDROLIGHT is the sum of the pure-water and particulate volume scattering functions. This sum is computed by weighting the pure water phase function ($\hat{\beta}_w$) and the particulate phase function ($\hat{\beta}_p$) by their respective scattering coefficients, or

$$\beta = b_w\hat{\beta}_w + b_p\hat{\beta}_p, \tag{3}$$

where b_w and b_p represent water and particulate scattering, respectively. The pure-water (Rayleigh-like) scattering phase function is from Einstein–Smoluchowski theory (Mobley 1994). An average Petzold (1972) phase function is used to characterize scattering by particulates (Mobley et al. 1993).

HYDROLIGHT is run with 10-nm resolution in the visible spectral region (250–700 nm) and 50-nm resolution in the 700–2500 nm region. The use of 50-nm resolution for the near-infrared bands results in more than a 50% decrease in computing time and less than a 1% change in transmission values compared to simulations performed with complete 10-nm resolution.

The incident radiance distribution provided to HYDROLIGHT is determined with the Santa Barbara DISORT Atmospheric Radiative Transfer (SBDART) model for the 250–2500 nm range (Ricchiazzi et al. 1998). SBDART combines Mie scattering code to compute plane-parallel cloud reflectance, low-resolution band models developed for LOWTRAN 7 to compute molecular absorption (Pierluissi and Marogoudakis 1986), a standard aerosol model, a Rayleigh scattering component, and the discrete ordinates radiative transfer equation solver of Stamnes et al. (1988). Irradiance val-

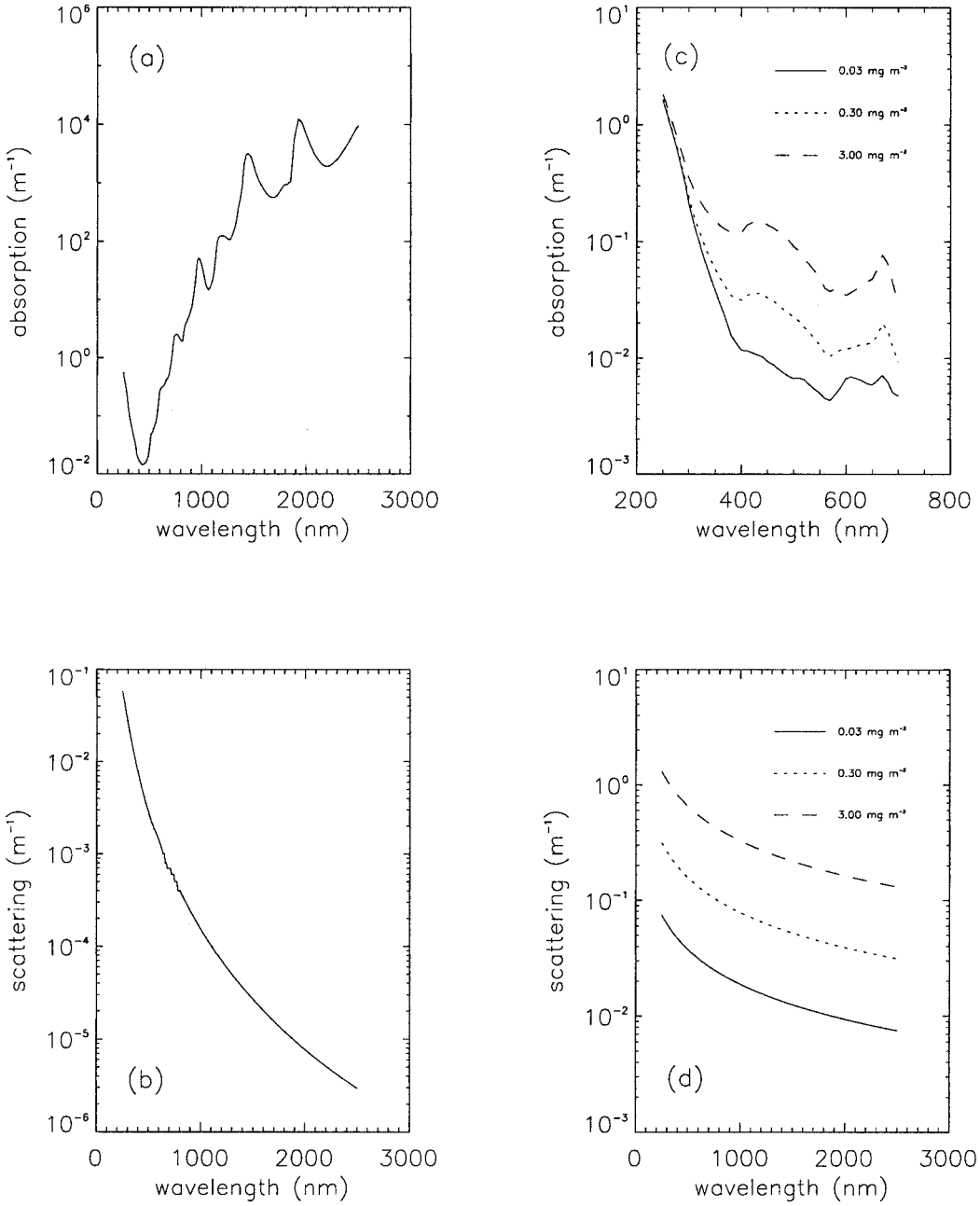

FIG. 1. Spectral absorption and scattering values used by HYDROLIGHT: (a) pure water absorption; (b) pure water scattering; (c) particulate absorption for chlorophyll values of 0.03, 0.3, and 3.0 mg m^{-3}; and (d) particulate scattering for 0.03, 0.3, and 3.0 mg m^{-3} chlorophyll.

ues from SBDART have been found to be in good agreement with surface irradiance measurements (Siegel et al. 1999; Ricchiazzi et al. 1998). Clouds are quantified by introducing a cloud index, CI, defined as one minus the ratio of downwelling irradiance to downwelling clear-sky irradiance at the sea surface (e.g., Gautier et al. 1980; Siegel et al. 1999). A cloud index of 0.20 corresponds to a 20% reduction in the incident solar flux from the clear sky value due to clouds. To arrive at the cloud indices used here, the optical thickness of the cloud layer at 550 nm (used by SBDART) was determined by trial and error for each combination of CI and solar zenith angle.

HYDROLIGHT requires both top and bottom boundary conditions. The Cox and Munk (1954) wave-slope statistics are used to simulate a wind-ruffled sea surface via a grid of triangular wave facets. Monte Carlo ray tracing is then used with Snell's law and Fresnel re-

flectance to compute the radiance transmittance and reflectance characteristics of the sea surface as a function of wind speed. These sea surface radiance transfer functions are the foundation of the surface boundary condition needed by HYDROLIGHT (Mobley 1994). Simulations of 20 000 photons for each directional quad (9.6×10^6 photons total) were used to determine the radiance reflectance distribution for a given incident direction as a function of wind speed. For the bottom boundary, an infinitely thick homogeneous layer of water with the same optical properties as water at the maximum depth of interest is used. The bidirectional radiance reflectance is computed by HYDROLIGHT for this layer, and is applied as a bottom boundary condition.

More than 150 HYDROLIGHT simulations are carried out for the upper 20 m with independent variables spanning the range of conditions found in open ocean waters. A maximum depth of 20 m is arbitrarily chosen and optical properties are considered uniform throughout the layer. Model runs are performed for upper-ocean chlorophyll concentrations (chl) of 0.03, 0.1, 0.3, 1.0, and 3.0 mg $m^{-3;}$ solar zenith angles (θ) of 0, 15, 30, 45, 60, and 75°; and cloud indices (CI) of 0, 0.2, 0.4, 0.6, and 0.9. For these 150 simulations the wind speed is set to 2 m s^{-1}. Transmission changes are mostly small (<0.01) when the wind speed is increased to 5 and 10 m s^{-1} for a subset of the above cases. The case of a clear sky, solar zenith angle 0°, and chlorophyll concentration 0.03 mg m^{-3} is characteristic of high incident irradiance, clear ocean conditions, and is subsequently referred to as the ''base case.'' Variations stated in absolute irradiance terms are based on a climatological surface irradiance of 200 W m^{-2}, characteristic of the WWP (Weller and Anderson 1996).

b. Computation of radiant heating rates

The average rate at which solar radiation heats an upper ocean layer of thickness z, or radiant heating rate (RHR), is

$$\mathrm{RHR}(z) = \frac{E_n(0^-) - E_n(z)}{\rho c_p z}, \tag{4}$$

where $E_n(0^-)$ is the total (spectrally integrated) net flux of solar radiation just beneath the sea surface, $E_n(z)$ is the total net solar flux at the base of the layer (depth z), ρ is the density of seawater, and c_p is the specific heat of seawater. Values of $E_n(0^-)$ and $E_n(z)$ can be parameterized from the total incident surface flux $E_d(0^+)$ through a solar transmission function, $\mathrm{Tr}(z)$, defined as

$$\mathrm{Tr}(z) = \frac{E_n(z)}{E_d(0^+)}. \tag{5}$$

Use of $E_d(0^+)$ in the transmission definition is desirable because it is easily measured and can be estimated from remotely sensed data (e.g., Gautier et al. 1980; Bishop and Rossow 1991; Weller and Anderson 1996). This definition contains effects of the air–sea interface, or sea surface albedo (α), defined as the ratio of upwelling to downwelling irradiance just above the sea surface. Using the definition of the net irradiance, $E_n(z) = E_d(z) - E_u(z)$, and conservation of energy across the interface, $E_n(0^+) = E_n(0^-)$, the sea surface albedo can be written as

$$\alpha = 1 - \frac{E_n(0^-)}{E_d(0^+)}. \tag{6}$$

All irradiance terms in Eqs. (4)–(6) are available from modeling results. Surface albedo relates to transmission as

$$\alpha = 1 - \mathrm{Tr}(0^-). \tag{7}$$

Both solar transmission and sea surface albedo have pronounced spectral signatures. Definitions for spectral transmission and albedo follow those of Eqs. (5)–(7) with the addition of wavelength (λ) dependence. Specifically, spectral transmission is defined as

$$\mathrm{Tr}(z, \lambda) = \frac{E_n(z, \lambda)}{E_d(0^+, \lambda)}, \tag{8}$$

and spectral albedo follows as

$$\alpha(\lambda) = 1 - \mathrm{Tr}(0^-, \lambda). \tag{9}$$

It is important to recognize that a transmission change for the deep-penetrating visible wavebands has different effects on radiant heating rates than a similar transmission change for the near-infrared wavebands, which are completely attenuated in the upper few meters (Ohlmann et al. 1996). Similarly, an albedo increase for visible wavebands will give a greater reduction in total irradiance just beneath the sea surface than a corresponding albedo increase in the near-infrared spectral region because visible wavebands contain more energy. Total albedo is not simply the integral of spectral albedo, but rather depends on the shape of the incident irradiance spectrum. The relationship between spectral and total albedo is expressed as

$$\alpha = \int_\lambda \alpha(\lambda) E_d(0^+, \lambda)\, d\lambda / E_d(0^+). \tag{10}$$

Spectral values must be addressed for a complete understanding of radiant heating rate variations.

3. Results

The complete set of HYDROLIGHT simulated profiles ($n = 150$) illustrates the expected range of solar transmission as a function of depth (Fig. 2). Transmission values at 1 cm and 5 m for a subset of the cases considered are given in Table 1. As seen in Fig. 2, solar transmission at 1 cm ranges from 0.69 for the high chl, high θ, low CI case, to 0.90 for the low chl, low θ, high CI case. The 0.21 transmission difference corresponds to a variation in net solar flux of 42 W m^{-2} (assuming

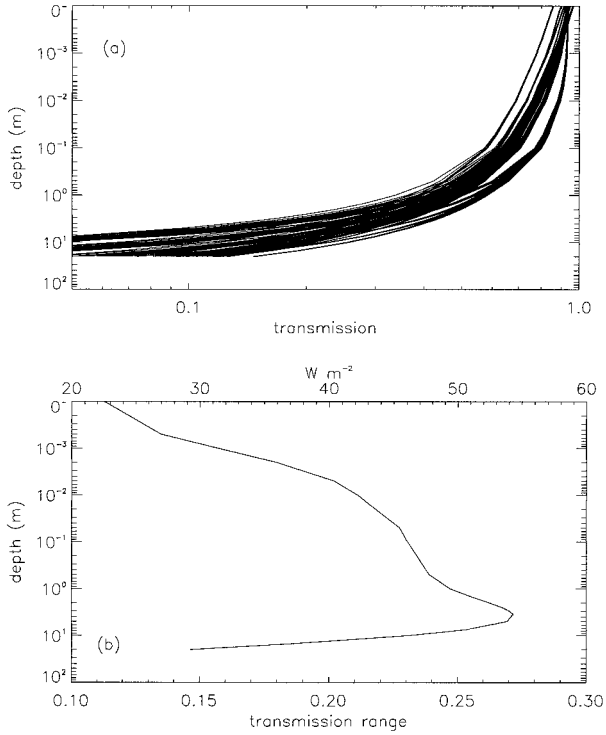

FIG. 2. (a) Total (spectrally integrated) solar transmission profiles for the HYDROLIGHT model runs considered here (chl = 0.03, 0.1, 0.3, 1.0, 3.0 mg m^{-3}; θ = 0°, 15°, 30°, 45°, 60°, 75°; CI = 0, 0.2, 0.4, 0.6, 0.9; ws = 2 m s^{-1}). (b) The range in transmission values covered by the set of profiles shown in (a). The range is also given in watts per square meter, based on a climatological surface irradiance of 200 W m^{-2}.

a daily mean surface irradiance of 200 W m^{-2}). Similarly, solar transmission at 5-m ranges from 0.10 to 0.37, corresponding to an absolute solar flux difference of 54 W m^{-2}. Contributions of chlorophyll concentration, cloud amount, solar zenith angle, and wind speed to these transmission variations are discussed below.

a. The chlorophyll concentration influence

Changes in solar transmission, Tr(z), from the base case (chl = 0.03 mg m^{-3}, θ = 0°, CI = 0) associated with chlorophyll perturbations (chl = 0.1, 0.3, 1.0 and 3.0 mg m^{-3}) are shown in Fig. 3. A tenfold increase in chlorophyll concentration results in less than a 0.01 change in solar transmission for the upper meter, which corresponds to a solar flux difference of only 2 W m^{-2} (for a climatological surface irradiance of 200 W m^{-2}). This same increase in chlorophyll concentration is responsible for a decrease in solar transmission of more than 0.05 (10 W m^{-2}) at depths beyond 10 m. A chlorophyll increase to 3.0 mg m^{-3} results in solar transmission decreases of less than 0.01 within the upper 10 cm and more than 0.15 (30 W m^{-2}) near 10 m. The transmission changes with elevated chlorophyll concentration are due primarily to increased attenuation in the visible wavebands and slightly to increased surface albedo through backscattering.

Transmission spectra at 1 and 10 m for the various chlorophyll concentrations illustrate how the influence of chlorophyll on transmission is confined to the visible spectral region and how the chlorophyll influence becomes increasingly pronounced with depth (Fig. 4). Beyond ~700 nm, chlorophyll has little effect on solar transmission. The solar spectrum narrows with depth, becoming increasingly peaked in the blue-green wavebands, as the longer wavelengths are completely atten-

TABLE 1. Independent parameter values and solar transmission results for a subset of the modeled irradiance profiles. Sea surface albedo is given as total albedo, albedo for the visible spectral region (300–700 nm), and albedo for the near-infrared spectral region (700–2500 nm).

Chl conc. (chl) (mg m^{-3})	Cloud index (CI)	Zenith angle (θ) (deg)	Tr(z) (1 cm)	Tr(z) (5 m)	Albedo (α)	Albedo (300–700 nm)	Albedo (700–2500 nm)
0.03	0	0	0.784	0.294	0.033	0.039	0.025
0.1	0	0	0.784	0.282	0.033	0.040	0.025
0.3	0	0	0.783	0.259	0.034	0.041	0.025
1.0	0	0	0.782	0.213	0.035	0.043	0.025
3.0	0	0	0.780	0.145	0.036	0.046	0.025
0.03	0.2	0	0.783	0.289	0.050	0.056	0.044
0.03	0.4	0	0.798	0.297	0.057	0.062	0.051
0.03	0.6	0	0.824	0.313	0.059	0.063	0.052
0.03	0.9	0	0.897	0.366	0.060	0.064	0.053
0.03	0	15	0.782	0.290	0.033	0.040	0.026
0.03	0	30	0.779	0.285	0.036	0.044	0.028
0.03	0	45	0.762	0.268	0.052	0.059	0.044
0.03	0	60	0.736	0.252	0.083	0.089	0.077
0.03	0	75	0.692	0.236	0.141	0.135	0.147
0.03	0.9	75	0.884	0.359	0.060	0.064	0.053
3.0	0	75	0.686	0.097	0.145	0.143	0.147

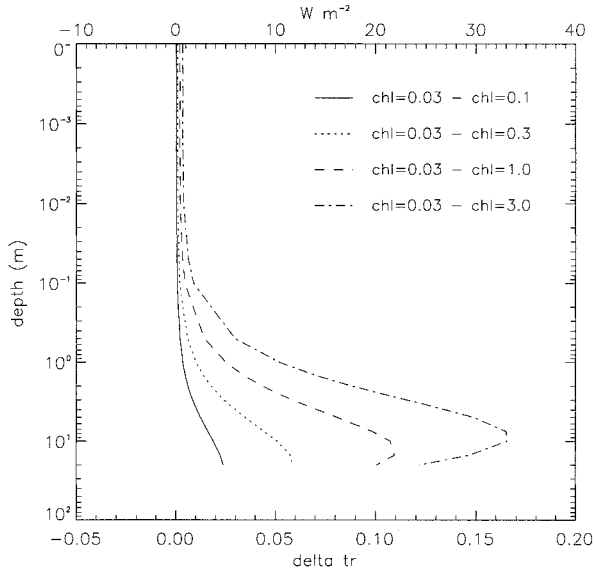

FIG. 3. Solar transmission differences between the base case (chl = 0.03 mg m^{-3}, $\theta = 0°$, CI = 0) and cases of increased chlorophyll concentration (chl = 0.1, 0.3, 1.0, 3.0 mg m^{-3}).

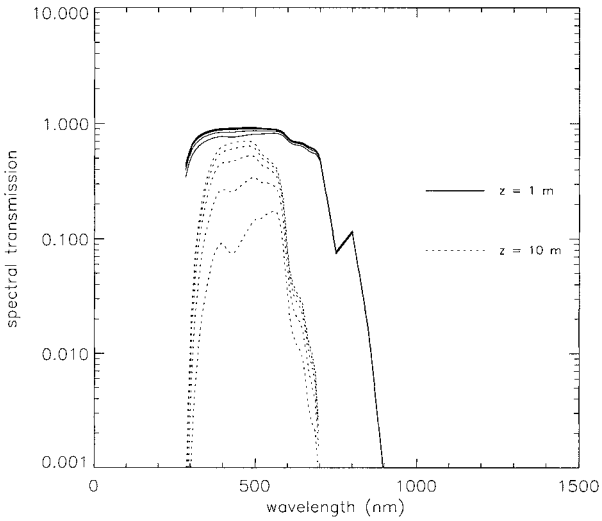

FIG. 4. Spectral transmission values for chlorophyll concentrations of 0.03, 0.1, 0.3, 1.0, and 3.0 mg m^{-3} at 1 (solid lines) and 10 (dashed lines) meters. Curves illustrate bandwidth narrowing with depth and the increased importance of chlorophyll on transmission at deeper depths.

uated within the upper meter. With a greater portion of the irradiance in the visible spectral region where attenuation is a function of chlorophyll biomass, the chlorophyll influence on solar transmission is more evident.

Spectral values of sea surface albedo computed with HYDROLIGHT for the different chlorophyll cases are shown in Fig. 5. Spectral albedo peaks above 0.06 near 400 nm for all chlorophyll cases considered. The reduction in albedo with increased chlorophyll between 400 and 450 nm is due to the chlorophyll absorption peak at 440 nm. The greatest change in spectral albedo (more than 30%) with chlorophyll lies between 500 and 600 nm, a region where scattering by phytoplankton is active (Mobley 1994). Spectral albedo beyond ~750 nm does not change with chlorophyll concentration. Overall, the hundredfold chlorophyll increase causes only a 0.003 increase in total albedo, corresponding to an <1 W m^{-2} decrease in energy available for upper ocean heating (Table 1; Fig. 3). Changes in available energy are in the visible wavebands, which have relatively small impacts on radiant heating rates because visible energy is distributed over large depths.

In summary, upper-ocean chlorophyll concentration plays a significant role in the regulation of solar transmission and radiant heating rates on mixed-layer depth scales (cf. Lewis et al. 1990; Morel and Antoine 1994; Siegel et al. 1995; Ohlmann et al. 1996, 1998). However, variations in chlorophyll concentration are of little importance when addressing radiant heating in the upper meter because a significant amount of the total energy exists beyond the chlorophyll sensitive wavebands. Chlorophyll effects on sea surface albedo are small and occur only within visible wavebands.

b. The cloud influence

The primary role of clouds is to reduce the amount of solar radiation reaching the sea surface (Fig. 6a). However, reductions in radiant heating rates are not simply proportional to reductions in the incident irradiance by clouds. This is due to the influence of clouds on the geometry and spectral composition of the incident irradiance. Figure 6b shows differences in incident spectral irradiance, normalized to the total incident irradiance, between the base and cloudy sky cases, relative to the base case. These values are computed by first

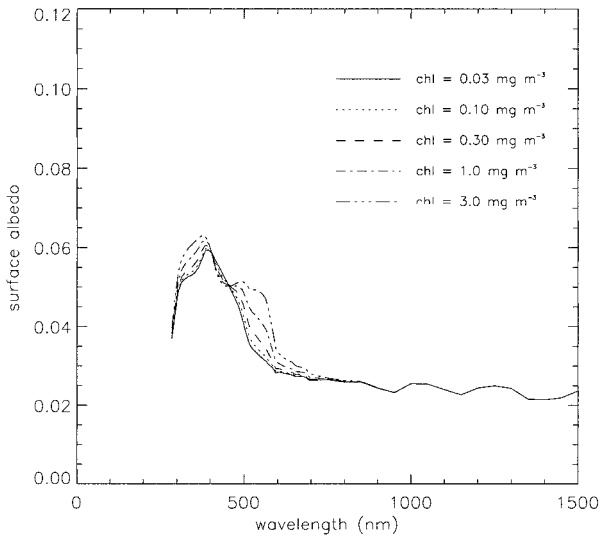

FIG. 5. Spectral albedo for the various chlorophyll concentration cases (chl = 0.03, 0.1, 0.3, 1.0, 3.0 mg m^{-3}) with $\theta = 0°$ and CI = 0.

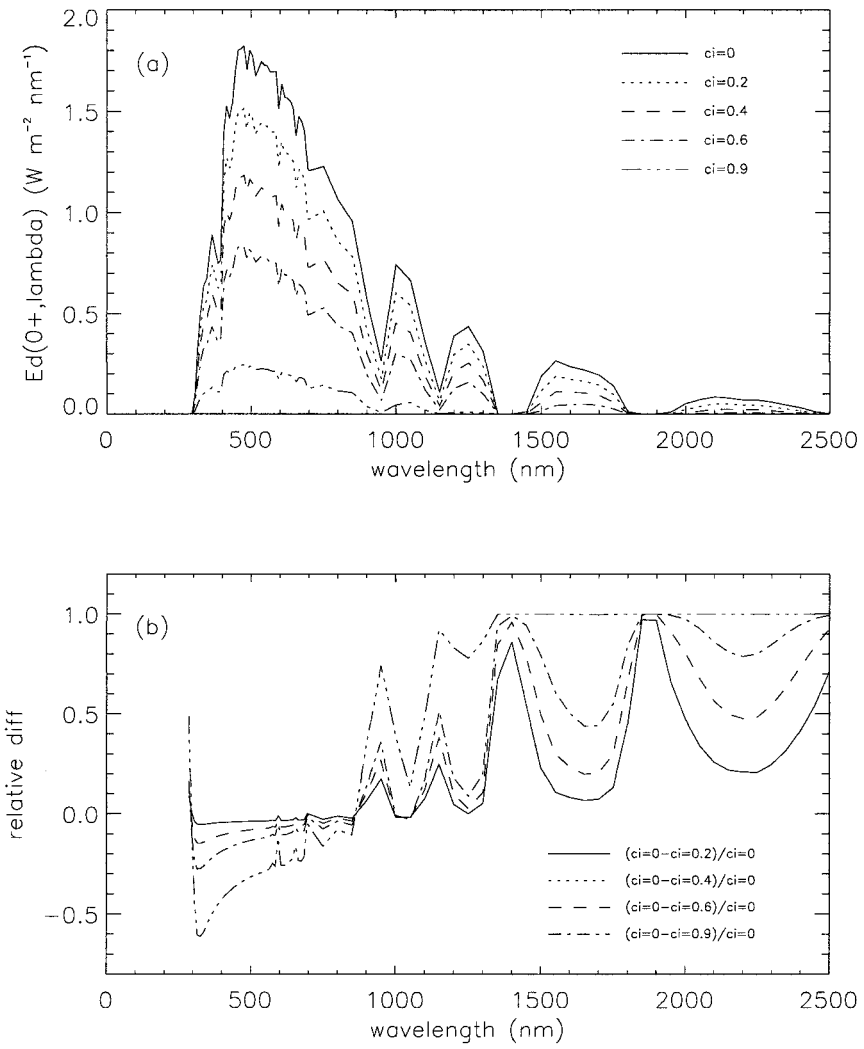

FIG. 6. (a) Irradiance spectra incident at the sea surface for the various cloud index cases (CI = clear sky, 0.2, 0.4, 0.6, 0.9) with chl = 0.03 mg m^{-3} and $\theta = 0°$. (b) Relative differences in spectral composition (spectral irradiance normalized to the total incident irradiance) between the clear sky base case and cases of varying cloud indices (CI = 0.2, 0.4, 0.6, 0.9). Cloud index increases are accompanied by a shift in energy from the near-infrared to shorter wavelengths relative to the total irradiance. Values <0 indicate an increase in energy from the base case.

normalizing the incident spectral irradiance for each of the cloud index cases by their respective total (spectrally integrated) fluxes. Differences in flux normalized spectral values from the clear sky base case are then calculated. Finally, these differences are normalized by base case values to give changes in flux normalized spectral values relative to those for a clear sky. Negative (positive) differences indicate an increase (decrease) in spectral irradiance (normalized to the broadband flux) due to clouds. An increase in the portion of the surface irradiance that exists in the deep penetrating visible spectral region and a corresponding decrease in near-infrared energy occurs with clouds. The spectral irradiance near 410 nm can increase by more than 50% (relative to the broadband irradiance) with clouds (Fig. 6b). For the clear sky case, 65% of the total incident solar flux exists in the 250 to 800 nm spectral region. This value increases to 70% and 83% for the 0.40 and 0.90 cloud index cases, respectively. The spectral shift is due primarily to a decrease in the contribution of Rayleigh scattering, relative to total attenuation, with clouds.

Solar transmission variations associated with perturbations in cloud amount (cloud index = 0.2, 0.4, 0.6, 0.9) are shown in Fig. 7. Transmission generally increases with cloud index as a greater portion of the incident irradiance exists in the deep-penetrating blue-green wavebands making Tr(clear) − Tr(cloud) differences negative. The total solar transmission difference between the clear sky and CI = 0.2 cases is negligible

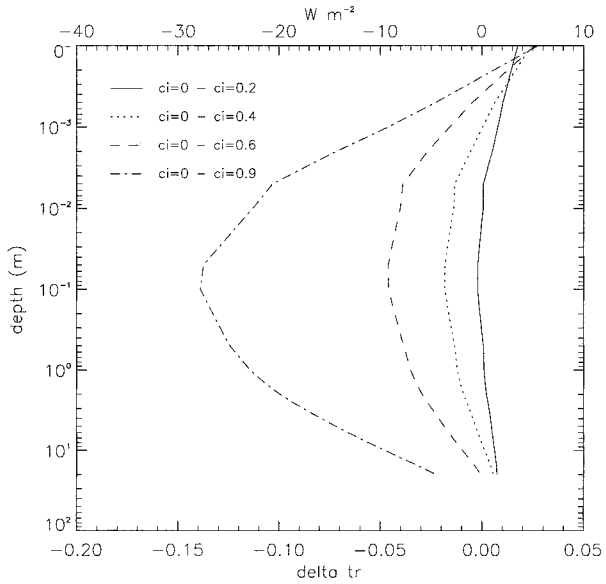

FIG. 7. Solar transmission differences between the base case (chl = 0.03 mg m^{-3}, $\theta = 0°$, CI = 0) and cases of increased cloud amount (CI = 0.2, 0.4, 0.6, 0.9). Values <0 indicate an increase in solar transmission from the base case.

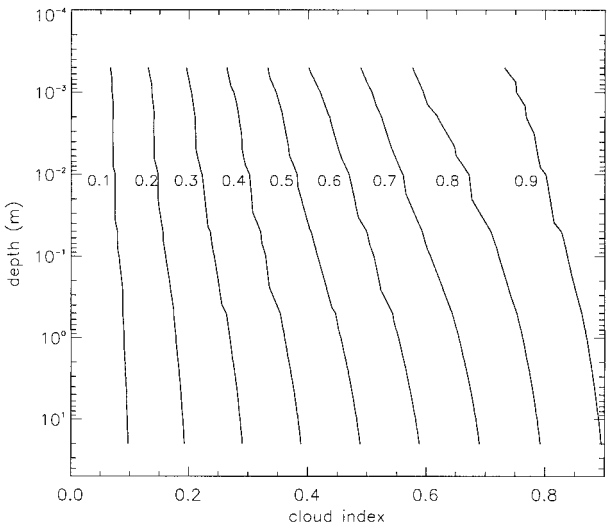

FIG. 8. Contours of radiant heating rate decreases as a function of cloud index and depth relative to clear sky heating rates. Decreases in radiant heating rates with clouds are greater than corresponding decreases in the incident surface irradiance (quantified by the cloud index).

(<0.005) beyond millimeter depth scales. For cloud indices of 0.6 and 0.9, solar transmission differences from the base case nearly reach 0.05 and 0.14 respectively at 10 cm, corresponding to absolute solar flux differences of 10 and 28 W m^{-2} (incident irradiance of 200 W m^{-2}). Transmission values at 1 cm and 5 m for various cloud index cases are given in Table 1. The changes in transmission with clouds are primarily manifest through alteration in spectral composition of the incident irradiance.

Changes in transmission and in the total incident irradiance must both be considered for quantification of instantaneous radiant heating variations with clouds. Figure 8 illustrates contours of radiant heating rate differences from the clear sky case normalized by the clear sky radiant heating rate as a function of cloud index and depth, or $[RHR_{clear} - RHR_{cloud}]/RHR_{clear}$. If the role of clouds were solely to reduce the incident irradiance, with no spectral or geometrical influences, cloud index would correspond to reductions in the incident irradiance and radiant heating rates. In this case contour lines in Fig. 8 would be vertical (following lines of constant cloud index). However, spectral and geometrical variations in the light field which accompany clouds make for radiant heating rate reductions which are greater than reductions in the incident irradiance (Fig. 8). For a cloud index of 0.4 (a 40% reduction in the total incident solar flux due to clouds), the radiant heating rate decrease for the upper 1 cm is nearly 53%, and the decrease in the upper 10 cm is greater than 47%.

The influence of clouds on the geometry of the light field is evidenced in transmission primarily through changes in the sea surface albedo. For small solar zenith angles, the addition of diffuse light with clouds increases the effective solar zenith angle resulting in increased albedo [decreased Tr(0^-); Eq. (7)] and a transmission decrease on millimeter depth scales (Fig. 7). For large solar zenith angles the opposite is true; the addition of diffuse light with increased cloud will decrease the effective solar zenith angle, resulting in an albedo decrease and a corresponding transmission increase on millimeter scales (figure not shown). Total sea-surface albedo values for various cloud indices and solar zenith angles are given in Table 1. Albedo is at a minimum (0.033) for the clear sky low solar zenith angle case and increases to 0.060 for the high cloud index low solar zenith angle case. When solar zenith angle is held constant at 75°, albedo decreases from 0.141 for the clear sky case to 0.060 for the CI = 0.9 case. An albedo decrease of 0.08 results in a 16 W m^{-2} increase in energy available for ocean radiant heating. Once the light field becomes sufficiently diffuse (CI ≥ 0.40), albedo remains relatively constant (~0.060) regardless of solar zenith angle (e.g., Payne 1972; Katsaros et al. 1985). Changes in spectral sea-surface albedo with cloud amount are greater in the red and near-infrared wavebands than in the visible spectral region (Fig. 9). Spectral albedo for the base case increases with wavelength to a maximum of 0.06 near 400 nm, and mostly fluctuates between 0.02 and 0.03 at wavelengths above 600 nm. Local minima in the near-infrared region are at wavebands where water vapor absorption is large (Liou 1980). Changes in total albedo with clouds come from a combination of changes in spectral albedo values and changes in spectral composition of the incident irradiance [Eq. (10)]. Overall, the influence of clouds on sur-

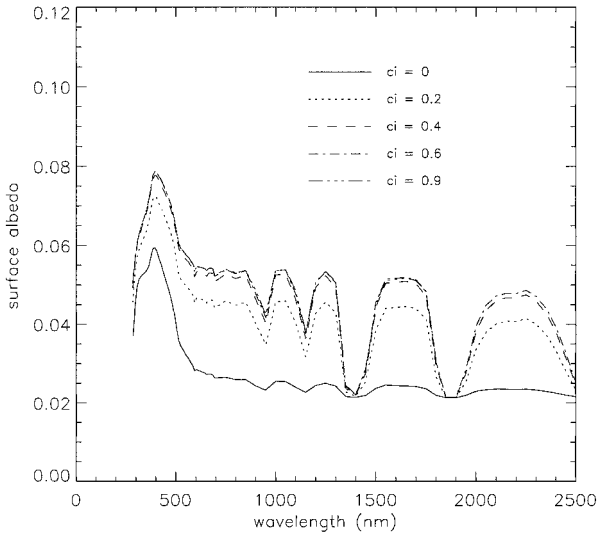

FIG. 9. Spectral albedo for the various cloud index cases (CI = clear sky, 0.2, 0.4, 0.6, 0.9) with chl = 0.03 mg m^{-3} and $\theta = 0°$.

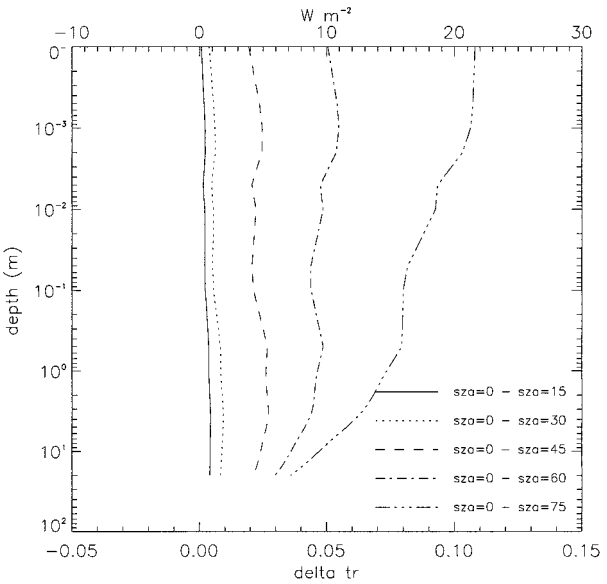

FIG. 10. Solar transmission differences between the base case (chl = 0.03 mg m^{-3}, $\theta = 0°$, CI = 0) and cases of increased solar zenith angle ($\theta = 15°, 30°, 45°, 60°, 75°$).

face albedo is small except at the largest solar zenith angles (Table 1).

In summary, clouds reduce the amount of solar energy incident at the sea surface, thereby reducing total ocean radiant heating. Clouds also influence total solar transmission by preferentially attenuating in the longer wavebands, altering the spectral composition of the incident irradiance and changing the structure of the incident radiance distribution. Certainly the net reduction in incident flux is the primary process regulating ocean radiant heating. However, changes in the incident radiance distribution can cause an albedo decrease of nearly 0.08 and a corresponding transmission change just beneath the sea surface. With more energy in the deep-penetrating visible wavebands (relative to total irradiance) under cloudy skies, the difference between reduction in surface irradiance and reduction in radiant heating rate for the top 10 cm of the ocean can exceed 10% (absolute flux 20 W m^{-2}).

c. The solar zenith angle influence

The role of solar zenith angle on transmission is similar to that of clouds, but smaller in magnitude. The primary effect of θ on upper-ocean radiant heating is alteration of the atmospheric path length, which regulates the total surface irradiance. In addition, changes in θ give rise to variations in the geometry of the radiance distribution and a slight recoloring of the incident spectrum. Differences in total solar transmission from the base case due to solar zenith angle perturbations are shown in Fig. 10. Transmission variations are small for small changes in θ but can be significant for large changes in θ. An increase in θ from 0° to 30° results in a reduction in solar transmission of less than 0.01 over the entire depth range. A 60° increase in θ gives a transmission decrease near 0.05 within the upper meter, corresponding to a 10 W m^{-2} decrease in the solar irradiance. Transmission differences associated with changes in θ are due primarily to sea surface albedo. This is illustrated by the curves in Fig. 10 that are nearly vertical in the near-surface and by albedo and transmission values given in Table 1 that show similar changes with θ increases.

To quantify effects of solar zenith angle on ocean radiant heating, changes in solar transmission and in the incident irradiance must be considered. Reductions in ocean radiant heating rates and the surface irradiance would be equivalent if changes in solar zenith angle simply altered the incident irradiance through path length. However, geometrical and spectral variations in the incident irradiance that accompany changes in the solar zenith angle cause radiant heating rate reductions which are slightly less than the corresponding reduction in incident irradiance. For example, an increases in θ from 0° to 60° (clear sky) results in a 57% decreases in the incident irradiance, but only a 54% decrease in the radiant heating rate for the top 1 mm. Differences between surface irradiance and radiant heating rate reductions for layers deeper than 1 cm are mostly negligible (<1%). Compared with cloud index, solar zenith angle plays a very small role in altering radiant heating rates relative to the surface irradiance.

Changes in spectral composition of the incident irradiance with solar zenith angle do exist (Fig. 11) but are negligible relative to spectral changes due to clouds (Fig. 6b). There is an effective transfer of energy from the near-ultraviolet wavebands primarily into the red and near-infrared wavebands <1750 nm as path length, and thus Rayleigh scattering, is increased. However, the

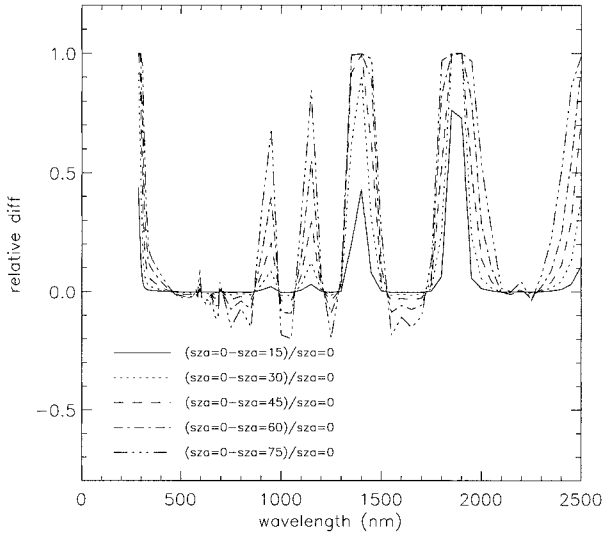

FIG. 11. Relative differences in spectral composition (spectral irradiance normalized to the incident irradiance) between the 0° solar zenith angle base case and cases of varying θ (θ = 15°, 30°, 45°, 60°, 75°). Solar zenith angle increases are accompanied by a small shift in energy into the green and red wavebands relative to the total irradiance. Values <0 indicate an increase in energy from the base case.

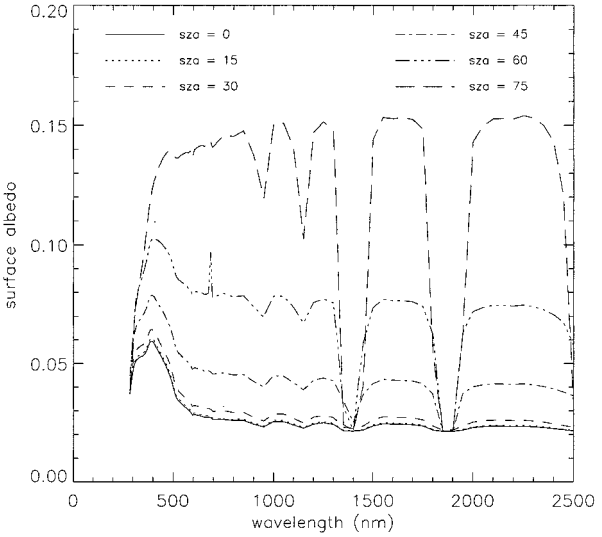

FIG. 12. Spectral albedo for the various solar zenith angle cases (θ = 0°, 15°, 30°, 45°, 60°, 75°, 90°) with chl = 0.03 mg m^{-3} and CI = 0.

fraction of the surface irradiance which exists in the 300 to 750 nm spectral range decreases only slightly, from 58.0% to 57.4%, when θ is increased from 0° to 75°. Spectral albedo for the various solar zenith angle cases is shown in Fig. 12. Values increase as 1/cosθ as is expected for a direct collimated light beam. Differences in spectral albedo are slightly greater in the red and near-infrared wavebands than in the visible. This decreases the amount of energy available to heat the upper few centimeters of the ocean relative to the total heat input and offsets the slight spectral enhancement of the near-infrared region. The effect of θ on spectral albedo shows a similar spectral shape, but is significantly less, when clouds are considered (see below). Differences in spectral transmission between the base case and perturbed θ cases remain relatively constant with depth suggesting effects of θ on transmission are conveyed almost entirely through surface albedo.

In summary, solar zenith angle variations largely influence the total surface irradiance, and thus upper ocean radiant heating rates, for clear sky conditions. Changes in the surface irradiance with θ are accompanied by variations in the radiance distribution and in spectral composition. Surface albedo, a function of radiance geometry, is the primary process in altering solar transmission with θ changes. Total albedo increases by 0.05 when solar zenith angle is increased from 0° to 60° for a clear sky, corresponding to a 10 W m^{-2} reduction in the amount of available energy for ocean radiant heating (based on a 200 W m^{-2} surface irradiance). Radiant heating rate variations (normalized by the incident irradiance) due to changes in solar zenith angle are greatest within the top few millimeters under clear skies, but are small overall.

d. The wind speed influence

Wind speed can influence solar transmission by changing sea surface slope statistics and thus surface albedo (Cox and Munk 1954). However, when wind speed is increased from 2 to 10 m s^{-1} for the clear sky, small θ, base case (chl = 0.03 mg m^{-3}, θ = 0°, CI = 0), transmission (albedo) changes are negligible (<0.007; Fig. 13; solid line). Surface albedo studies by Payne (1972) and Katsaros et al. (1985) indicate the role of wind speed may be more pronounced for large solar zenith angle values. This is considered below.

4. Discussion

a. Covarying factors

The results presented above consider variations in solar transmission from the base case (chl = 0.03 mg m^{-3}, θ = 0°, CI = 0) for perturbations in a single independent variable. In this section, effects of wind speed on solar transmission are considered for varying cloud amount and solar zenith angle cases, and transmission changes are assessed for competing effects of chlorophyll concentration, cloud amount, and solar zenith angle. Differences in solar transmission for various CI and θ combinations at wind speeds of 2 and 10 m s^{-1} are shown in Fig. 13. The only time wind speed has a pronounced effect on solar transmission is for clear sky, large solar zenith angle ($\theta \geq 75°$) cases. An increase in wind speed from 2 to 10 m s^{-1} for the clear sky, 75° θ case gives a maximum transmission increase of 0.03 (6 W m^{-2}) as the surface albedo is reduced through

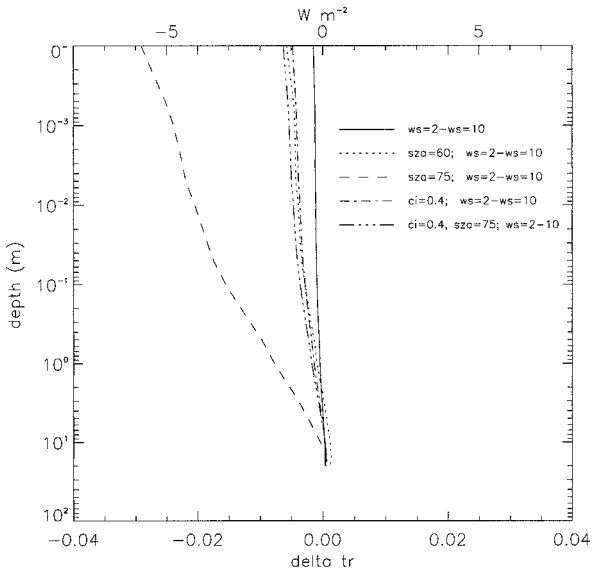

FIG. 13. Solar transmission differences between wind speed cases (2 and 10 m s^{-1}) for various combinations of θ and CI ($\theta = 0°$, CI = 0, $\theta = 60°$, CI = 0; $\theta = 75°$, CI = 0; $\theta = 0°$, CI = 0.4; $\theta = 75°$, CI = 0.4). In all instances chl = 0.03 mg m^{-3}. Values <0 indicate an increase in transmission from the base case. Variations in wind speed significantly influence transmission only during periods when the sky is clear and solar zenith angle is large.

changes in the angle between incident photons and wave facets. The largest variations in solar transmission caused by wind speed are still small compared to transmission variations associated with chlorophyll concentration, cloud amount, and solar zenith angle changes. The sensitivity to wind speed examined here does not consider the role of gravity waves or whitecapping.

Differences in solar transmission from the base case associated with combined changes in chlorophyll concentration, solar zenith angle, and cloud amount are illustrated in Fig. 14. As expected, chlorophyll concentrations have little influence on solar transmission within the uppermost 1 m regardless of solar angle and clouds. Beneath ~1 m effects of chlorophyll concentration on solar transmission are significant. Chlorophyll concentration effects are reduced by solar zenith angle increases and enhanced by clouds (Fig. 14a). The enhanced effect of chlorophyll under cloudy skies is due to the role of clouds in shaping the incident irradiance spectrum. As energy in the visible wavebands (relative to the total irradiance) increases with clouds, total solar transmission beyond ~1 m decreases because there is more energy in the wavebands attenuated by chlorophyll. The solar transmission difference between the chl = 0.03 and chl = 3.0 mg m^{-3} cases can be as much as 0.05 (10 W m^{-2}) greater under completely overcast skies. The reduced effect of chlorophyll concentration on solar transmission with increased solar zenith angle occurs only for clear skies, is due to surface albedo, and is small. An increase in surface albedo gives a slight reduction in visible energy (relative to the total irradiance), thus damping the effect of chlorophyll effects.

Changes in solar zenith angle have little influence on solar transmission under cloudy skies. This follows from the role of clouds in generating diffuse light that reduces effects of solar zenith angle. While an increase in solar zenith angle from 0° to 60° under clear skies gives a transmission decrease exceeding 0.05 (Fig. 10), a corresponding zenith angle change under cloudy skies results in a transmission decrease of less than 0.02 (Fig. 14b). In contrast, changes in solar transmission associated with cloud amount perturbations are enhanced with increased solar zenith angle (Fig. 14c). Cloud effects on spectral composition of the incident irradiance (relative to the total incident irradiance) are amplified by increased atmospheric path length. The transmission difference between the clear sky and CI = 0.6 cases increases from <0.05 for the 0° θ case (Fig. 7) to nearly .012 for the 75° θ case (Fig. 14c). This transmission change of ~0.07 corresponds to an absolute solar flux of 14 W m^{-2}. While the sensitivity of solar transmission to changes in solar zenith angle is significant only under clear skies, cloud effects on solar transmission are significant for the entire range of solar zenith angles and increase with zenith angle.

The chlorophyll concentration, cloud amount, solar zenith angle, and wind speed influences on solar transmission along with their interdependencies are summarized in Table 2. Chlorophyll concentration and cloud amount have the largest overall influence on solar transmission. Chlorophyll acts to reduce solar transmission at depths beyond ~1 m. In contrast, clouds primarily enhance solar transmission in the millimeter to 10-m depth range. The cloud influence increases slightly with solar zenith angle and the chlorophyll concentration influence increases slightly with cloud amount. Solar zenith angle can also have first-order effects on solar transmission, but only during clear sky periods. Solar zenith angle influences transmission primarily through changes in sea surface albedo. Under cloudy skies solar zenith angle changes have reduced effects on the geometric structure of the incident light field, and thus have little influence on solar transmission. The effects of wind speed on solar transmission are greatest during clear sky, large solar zenith angle periods, but are small overall.

b. Sea surface albedo

Sea surface albedo values have been parameterized from field data as a function of atmospheric transmittance (defined as the ratio of downward irradiance incident at the sea surface to irradiance at the top of the atmosphere) and solar zenith angle (Payne 1972). The table of albedo values presented by Payne allows direct comparison between the simulated albedo values given here and observationally based albedo values. Linear regression analysis between the complete set of simulated albedo values and corresponding values from

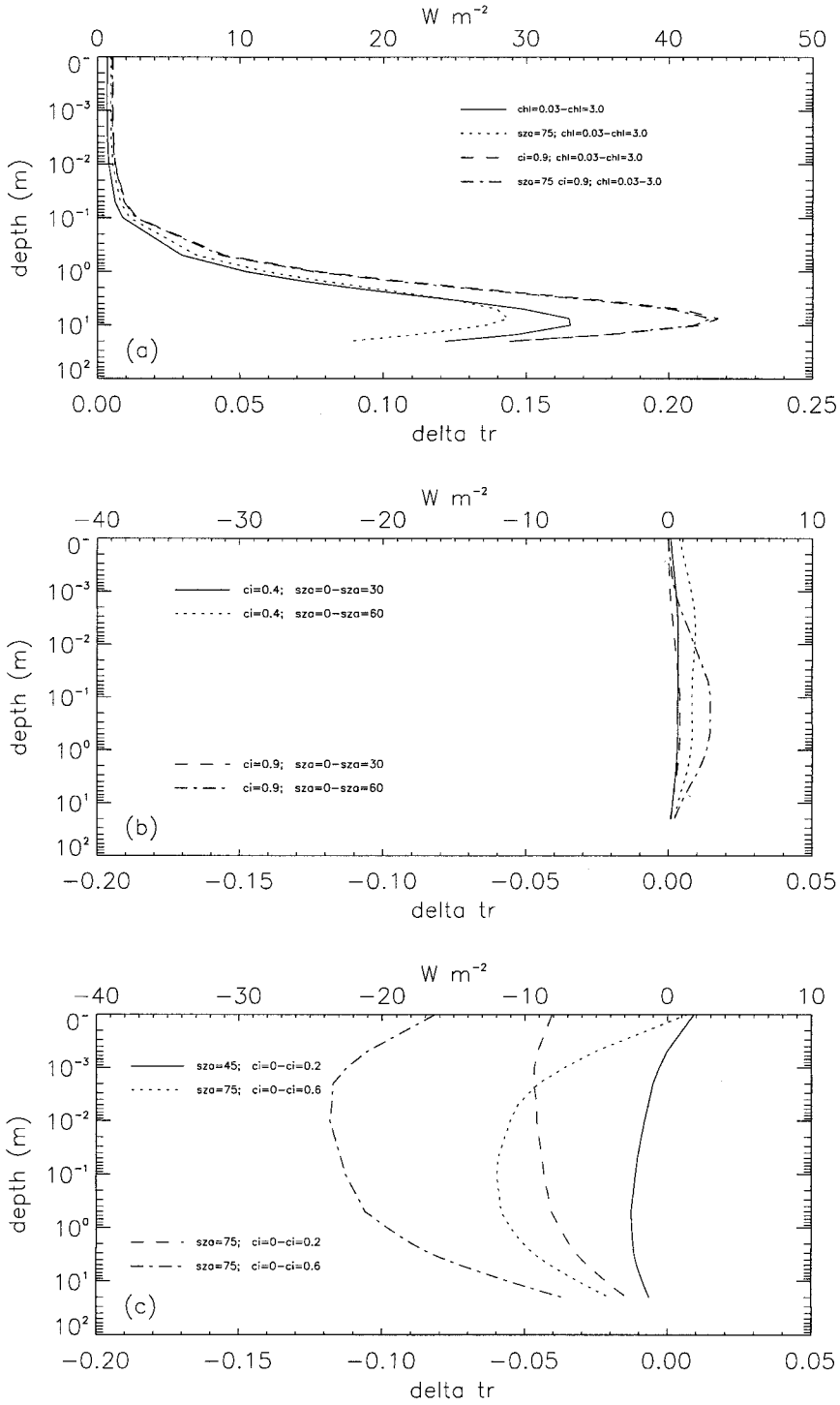

FIG. 14. Solar transmission differences from the base case (chl = 0.03 mg m^{-3}, $\theta = 0°$, CI = 0 (a) for increased chl and various CI and θ values, (b) for increased θ and various CI, and (c) for increased CI and various θ. Values <0 indicate an increase in transmission from the base case. Values of chl, CI, and θ for each curve are indicated only if different from the base case.

TABLE 2. Summary of chlorophyll concentration (chl), cloud index (CI), solar zenith angle (θ), and wind speed (WS) influences on solar transmission. Implications are indicated by the depth scale where "E_n (mixed layer base)" indicates penetration through the mixed layer ($z \sim 10$ m), "warm layer" indicates a warm-layer correction ($z \sim 1$ m), and "cool skin" denotes a cool-skin correction ($z < 1$ mm).

Factor	Influence	Conditions	Parameter	Implications/comments
chl	Strong	All	Tr($z > 1$ m)	E_n (mixed layer base), warm layer; enhanced with CI increases.
chl	Weak	All	α	None.
CI	Strong	All	Tr($z < 10$ m)	Warm layer, cool skin; CI effects are enhanced with θ increases.
CI	Strong	$\theta > 60°$	α	The CI influence on α can be moderate for θ near 0°.
θ	Strong	Clear sky	Tr($z < 10$ m)	Warm layer, cool skin; θ effects on Tr($z >$ 10 m) can be moderate.
θ	Strong	Clear sky	α	The θ influence on Tr is through α.
WS	Weak	All	Tr(z)	Can be moderate at $z < 1$ m for clear sky, large θ conditions.
WS	Weak	All	α	The WS influence on Tr is through α.

Payne's (1972) study shows significant agreement, with simulated values underestimating (overestimating) Payne's values when albedo is large (small; Fig. 15). Values agree to within 10% for more than two-thirds of the cases examined, corresponding to an absolute solar flux difference less than 2 W m^{-2} (for a climatological surface irradiance of 200 W m^{-2} and albedo values <0.10). The largest albedo differences occur for the 0° θ, 0.2 CI cases for which model results overestimate Payne's albedo values by just less than 30%. In the absence of near-surface transmission data, comparison of modeled albedo values with Payne's (1972) observationally based values provides the best possible way of validating the model results used here.

The definition of solar transmission used here relates the net irradiance at depth to the downwelling irradiance incident at the sea surface and is convenient because it allows $E_n(z)$, the value of interest, to be directly related to an accurately measurable parameter [$E_d(0^+)$]. When transmission is defined in this manner, sea surface albedo is implicitly included, but can easily be isolated [Eq. (7)]. Chlorophyll concentration, cloud amount, solar zenith angle, and wind speed all influence surface albedo. However, the importance of these parameters is substantially different than for transmission beyond the top millimeter (Table 2). Solar zenith angle has the greatest influence on surface albedo, but only for clear sky conditions. A solar zenith angle increase from 0° to 75° under clear skies results in a surface albedo rise of more than 0.1 (20 W m^{-2}; Fig. 10). This same increase in θ gives a surface albedo change of less than 0.01 for a cloudy sky (CI > 0.4; Fig. 14b).

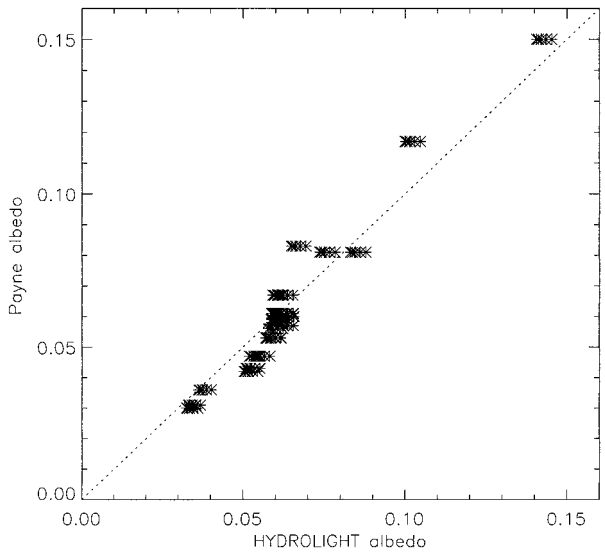

FIG. 15. Sea surface albedo from radiative transfer model runs compared with parameterized values from Payne (1972; $n = 150$, $r^2 = 0.94$, rms error = 0.006).

Cloud index can also have a first-order influence on surface albedo, but only for large solar zenith angles. When the solar zenith angle is 75° and cloud index is increased from the clear sky case to 0.6, surface albedo decreases by more than 0.08 (16 W m^{-2}; Fig. 14c). This same increase in cloud index gives an albedo rise of $\sim$0.025 when θ is 0° (Fig. 7). Wind speed effects on surface albedo are greatest during clear sky, large solar zenith angle periods but are still small compared with cloud index and solar zenith angle influences. When wind speed is increased from 2 to 10 m s^{-1} (clear sky, $\theta = 75°$) albedo decreases by nearly 0.03 (6 W m^{-2}; Fig. 13). This same wind speed increase gives an albedo change of less than 0.01 when $\theta \leq 60°$ or when CI is increased beyond 0.2. Although a change in upper-ocean chlorophyll concentration alters the amount of solar radiation that is scattered back to the atmosphere from beneath the sea surface, the influence of chlorophyll concentration on surface albedo is nearly negligible. A chlorophyll increase from 0.03 to 3.0 mg m^{-3} results in an albedo increases that are less than 0.005 (1 W m^{-2}; Fig. 3).

5. Conclusions

Radiative transfer modeling results demonstrate that in-water solar fluxes can vary by as much as 40 W m^{-2}

at depth within the upper few meters of the ocean (based on an incident irradiance of 200 W m^{-2}). Such variations in solar transmission are due primarily to upper-ocean chlorophyll concentration and cloud amount. Solar zenith angle and wind speed have a second-order influence on solar transmission. However, solar zenith angle effects can be significant during clear sky periods. Chlorophyll concentration affects the attenuation of solar radiation within the visible spectral wavebands and thus has little influence on solar transmission within the top meter where near-infrared energy is substantial. Clouds alter the radiance distribution through the direct to diffuse light ratio and the spectral shape of the incident irradiance relative to the total irradiance. Clouds increase solar transmission in the upper few meters by causing a relatively greater portion of the incident solar energy to exist in the deep-penetrating visible wavebands. Solar zenith angle and wind speed both influence solar transmission through sea surface albedo. Thus the effects of solar zenith angle and wind speed on transmission are greatest just beneath the sea surface and decrease with depth.

Solar transmission has been defined here as the ratio of the net solar flux at depth to the total downwelling solar flux incident at the sea surface [Eq. (5)] so that the role of sea surface albedo is included. This definition is convenient because it enables determination of $E_n(z)$ from $E_d(0^+)$, a readily available parameter that can be directly measured with a high degree of accuracy or parameterized from remotely sensed cloud data. Improved parameterizations of sea surface albedo will necessarily emerge with future solar transmission parameterizations that must rely upon upper ocean chlorophyll concentration, cloud amount and solar zenith angle. A companion paper (Ohlmann and Siegel 2000) uses the simulated profiles and results presented here to develop an all-condition empirical parameterization, which defines solar transmission in terms of upper ocean chlorophyll concentration and cloud index for cloudy sky periods, and chlorophyll and solar zenith angle for clear sky periods. Incorporating such a physically and biologically based solar transmission parameterization into upper ocean models will ultimately reduce uncertainties in SST prediction, especially for high illumination, low wind speed conditions.

Acknowledgments. Catherine Gautier kindly supplied the SBDART model. Discussions with Steve Anderson, Bill O'Hirok, Paul Ricchiazzi, and Bob Weller were extremely helpful in guiding this study. Two anonymous reviewers provided thoughtful comments that made for an improved manuscript. We gratefully acknowledge support from the National Science Foundation (OCE-9525856) and NASA (NAGW-3145). The development of HYDROLIGHT by author CDM is supported by the Environmental Optics Program of the Office of Naval Research (N00014-97-C-0024).

REFERENCES

Bishop, J. K. B., and W. B. Rossow, 1991: Spatial and temporal variability of global surface solar irradiance. *J. Geophys. Res.*, **96,** 16 839–16 858.

Brainerd, K. E., and M. C. Gregg, 1997: Turbulence and stratification on the Tropical Ocean-Global Atmosphere–Coupled Ocean Atmosphere Response Experiment microstructure pilot cruise. *J. Geophys. Res.*, **102,** 10 437–10 455.

Charlock, T. P., 1982: Mid-latitude model analysis of solar radiation, the upper layers of the sea, and seasonal climate. *J. Geophys. Res.,* **87,** 8923–8930.

Cox, C., and W. Munk, 1954: Statistics of the sea surface derived from sun glitter. *J. Mar. Res.,* **13,** 198–227.

Cronin, M. F., and M. J. McPhaden, 1997: The upper ocean heat balance in the western equatorial Pacific warm pool during September–December 1992. *J. Geophys. Res.,* **102,** 8533–8553.

Denman, K. L., 1973: A time-dependent model of the upper ocean. *J. Phys. Oceanogr.,* **3,** 173–184.

Fairall, C. W., E. F. Bradley, J. S. Godfrey, G. A. Wick, J. B. Edson, and G. S. Young, 1996a: Cool-skin and warm-layer effects on sea surface temperature. *J. Geophys. Res.*, **101,** 1295–1308.

——, ——, D. P. Rogers, J. B. Edson, and G. S. Young, 1996b: Bulk parameterization of air–sea fluxes for Tropical Ocean-Global Atmosphere–Coupled Ocean Atmosphere Response Experiment. *J. Geophys. Res.*, **101,** 3747–3764.

Gautier, C., G. R. Diak, and S. Masse, 1980: A simple model to estimate incident solar radiation at the sea surface. *J. Appl. Meteor.,* **19,** 1005–1012.

Gordon, H. R., 1989: Dependence of the diffuse reflectance of natural waters on the sun angle. *Limnol. Oceanogr.,* **34,** 1484–1489.

——, and A. Morel, 1983: Remote assessment of ocean color for interpretation of satellite visible imagery, a review. *Lecture Notes on Coastal and Estuarine Studies,* Vol. 4. Springer-Verlag, 114 pp.

Hale, G. M., and M. R. Querry, 1973: Optical constants of water in the 200-nm to 200-μm wavelength region. *Appl. Opt.,* **12,** 555–563.

Jerlov, N. G., 1976: *Marine Optics.* Elsevier, 229 pp.

Kantha, L. H., and C. A. Clayson, 1994: An improved mixed-layer model for geophysical applications. *J. Geophys. Res.,* **99,** 25 235–25 266.

Katsaros, K. B., L. A. McMurdie, R. J. Lind, and J. E. DeVault, 1985: Albedo of a water surface, spectral variation, effects of atmospheric transmittance, sun angle and wind speed. *J. Geophys. Res.,* **90,** 7313–7321.

Kirk, J. T. O., 1984: Dependence of relationship between inherent and apparent optical properties of water on solar altitude. *Limnol. Oceanogr.,* **29,** 350–356.

Kraus, E. B., 1972: *Atmosphere–Ocean Interaction.* Clarendon, 275 pp.

Lewis, M. R., M.-E. Carr, G. C. Feldman, W. Esaias, and C. McClain, 1990: Influence of penetrating solar radiation on the heat budget of the equatorial Pacific Ocean. *Nature,* **347,** 543–545.

Liou, K. N., 1980: *An Introduction to Atmospheric Radiation.* Academic Press, 392 pp.

Mobley, C. D., 1989: A numerical model for the computation of radiance distributions in natural waters with wind roughened surfaces. *Limnol. Oceanogr.,* **34,** 1473–1483.

——, 1994: *Light and Water.* Academic Press, 592 pp.

——, and Coauthors, 1993: Comparison of numerical models for computing underwater light fields. *Appl. Opt.,* **32,** 7484–7505.

Morel, A., 1988: Optical modeling of the upper ocean in relation to its biogenous matter content (case I waters). *J. Geophys. Res.,* **93,** 10 749–10 768.

——, 1991: Light and marine photosynthesis: A spectral model with geochemical and climatological implications. *Progress in Oceanography,* Vol. 26, Pergamon, 263–306.

——, and D. Antoine, 1994: Heating rate within the upper ocean in

relation to its bio-optical state. *J. Phys. Oceanogr.,* **24,** 1652–1665.

Nann, S., and C. Riordan, 1991: Solar spectral irradiance under clear and cloudy skies: measurements and a semiempirical model. *J. Appl. Meteor.,* **30,** 447–462.

Ohlmann, J. C., and D. A. Siegel, 2000: Ocean radient heating. Part II: Parameterizing solar radiation transmission through the upper ocean. *J. Phys. Oceanogr.,* **30,** 1849–1865.

——, ——, and C. Gautier, 1996: Ocean mixed layer radiant heating and solar penetration: A global analysis. *J. Climate,* **9,** 2265–2280.

——, ——, and L. Washburn, 1998: Radiant heating of the western equatorial Pacific during TOGA-COARE. *J. Geophys. Res.,* **103,** 5379–5395.

Paulson, C. A., and J. J. Simpson, 1977: Irradiance measurements in the upper ocean. *J. Phys. Oceanogr.,* **7,** 953–956.

——, and ——, 1981: The temperature difference across the cool skin of the ocean. *J. Geophys. Res.,* **86,** 11 044–11 054.

Payne, R. E., 1972: Albedo of the sea surface. *J. Atmos. Sci.,* **29,** 959–970.

Petzold, T. J., 1972: Volume scattering functions for selected natural waters. Scripps Inst. Oceanogr. Visibility Lab. SIO Ref. 72–78, 79 pp. [Available from Scripps Institute of Oceanography, University of California, San Diego, La Jolla, CA 92093.]

Pierluissi, J. H., and C. E. Maragoudakis, 1986: Molecular transmission band models for LOWTRAN. AFGL Tech. Rep. 86-0272, 63 pp. [Available from Air Force Geophysical Lab., Hanscom Air Force Base, MA 01731.]

Preisendorfer, R. W., and C. D. Mobley, 1986: Albedos and glitter patterns of a wind roughened sea surface. *J. Phys. Oceanogr.,* **16,** 1293–1316.

Prieur, L., and S. Sathyendranath, 1981: An optical classification of coastal and oceanic waters based on the specific spectral absorption curves of phytoplankton pigments, dissolved organic matter, and other particulate materials. *Limnol. Oceanogr.,* **26,** 671–689.

Ricchiazzi, P., S. Yang, C. Gautier, and D. Sowle, 1998: SBDART: A research and teaching software tool for plane-parallel radiative transfer in the earth's atmosphere. *Bull. Amer. Meteor. Soc.,* **79,** 2101–2114.

Schneider, N., T. Barnett, M. Latif, and T. Stockdale, 1996: Warm pool physics in a coupled GCM. *J. Climate,* **9,** 219–239.

Siegel, D. A., and T. D. Dickey, 1987: On the parameterization of irradiance for open ocean photoprocesses. *J. Geophys. Res.,* **92,** 14 648–14 662.

——, J. C. Ohlmann, L. Washburn, R. R. Bidigare, C. Nosse, E. Fields, and Y. Zhou, 1995: Solar radiation, phytoplankton pigments and radiant heating of the equatorial Pacific warm pool. *J. Geophys. Res.,* **100,** 4885–4891.

——, T. Westberry, and J. C. Ohlmann, 1999: Cloud color and ocean radiant heating. *J. Climate,* **12,** 1101–1116.

Simonot, J. Y., and H. Le Treut, 1986: A climatological field of mean optical properties of the world ocean. *J. Geophys. Res.,* **91,** 6642–6646.

Simpson, J. J., and C. A. Paulson, 1979: Mid-ocean observations of atmospheric radiation. *Quart. J. Roy. Meteor. Soc.,* **105,** 487–502.

——, and T. D. Dickey, 1981: The relationship between downward irradiance and upper ocean structure. *J. Phys. Oceanogr.,* **11,** 309–323.

Smith, R. C., and K. S. Baker, 1978, Optical classification of natural waters. *Limnol. Oceanogr.,* **23,** 260–267.

——, and ——, 1981: Optical properties of the clearest natural waters. *Appl. Opt.,* **20,** 177–184.

Stamnes, K., S. C. Tsay, W. J. Wiscombe, and K. Jayaweera, 1988: Numerically stable algorithm for discrete ordinate method radiative transfer in multiple scattering and emitting layered media. *Appl. Opt.,* **27,** 2502–2509.

Webster, P. J., and R. Lukas, 1992: TOGA COARE: The Coupled Ocean–Atmosphere Response Experiment. *Bull. Amer. Meteor. Soc.,* **73,** 1377–1416.

Weller, R. A., and S. P. Anderson, 1996: Surface meteorology and air–sea fluxes in the western equatorial Pacific Warm Pool during the TOGA Coupled Ocean–Atmosphere Response Experiment. *J. Climate,* **9,** 1959–1991.

Wijesekera, H. W., and M. C. Gregg, 1996: Surface layer response to weak winds, westerly bursts, and rain squalls in the western Pacific Warm Pool. *J. Geophys. Res.,* **101,** 977–997.

Woods, J. D., W. Barkmann, and A. Horch, 1984: Solar heating of the oceans—Diurnal, seasonal and meridional variation. *Quart. J. Roy. Meteor., Soc.,* **110,** 633–656.

Zaneveld, J. R., and R. W. Spinrad, 1980: An arc tangent model of irradiance in the sea. *J. Geophys. Res.,* **85,** 4919–4922.